International Forum on Aeroelasticity and Structural Dynamics
IFASD 2026
16-19 June 2026, Göttingen, Germany

DESIGN OF A SWEPT WING MODEL FOR THE INVESTIGATION OF SEMI-ACTIVE FLUTTER SUPPRESSION IN TRANSONIC FLOW

Jens Nitzsche[1], Johannes Dillinger[1], Diliana Friedewald[1], Jan Himisch[2], Moritz Schmidt[3]

[1]Institute of Aeroelasticity, German Aerospace Center (DLR)
37073 Göttingen, Germany

[2]Institute of Aerodynamics and Flow Technology, German Aerospace Center (DLR)
38108 Braunschweig, Germany

[3]Systemhaus Technik, German Aerospace Center (DLR)
38108 Braunschweig, Germany

Keywords: flutter, unsteady aerodynamics, transonic dip, contour bumps, wind tunnel experiment

Abstract: Experimental investigations of passive flutter-suppression concepts on realistic swept transonic wings require suitable benchmark configurations exhibiting a well-defined classical flutter mechanism. No such model was available for the DNW Transonic Wind Tunnel Göttingen (DNW-TWG). The present work therefore describes the numerical development of a new swept transonic benchmark wing intended for the experimental investigation of semi-active flutter suppression concepts. A hierarchical design workflow combining low-fidelity structural pre-design with high-fidelity CFD-based aeroelastic analyses was employed. The resulting configuration exhibits a classical flutter mechanism governed by the interaction of the second bending and first torsional modes together with a pronounced transonic dip within the operating envelope of the DNW-TWG. Good agreement is obtained between fully coupled nonlinear fluid–structure interaction simulations and the corresponding linearized frequency-domain flutter predictions. A first numerical investigation demonstrates that localized contour bumps can substantially increase the flutter boundary within the transonic dip while leaving the low-Mach-number behavior largely unaffected. The resulting benchmark provides the basis for the planned wind-tunnel campaign and constitutes a new validation case for CFD-based aeroelastic prediction methods.

1 INTRODUCTION

Future transport aircraft are expected to employ increasingly slender, high-aspect-ratio wings in order to improve aerodynamic efficiency. As structural flexibility increases, flutter becomes an increasingly important design constraint, particularly in the transonic regime, where the flutter boundary often exhibits a pronounced local minimum as a function of Mach number, commonly referred to as the *transonic dip*. From an engineering perspective, it is therefore highly desirable to alleviate or shift this transonic dip without fundamentally modifying the wing structure or compromising aerodynamic performance.

Among the concepts proposed in recent years, passive (or semi-active) aerodynamic devices have attracted considerable interest as an alternative to complex active control systems. By introducing localized modifications of the aerodynamic surface, such devices alter the stationary flow field and may improve the flutter boundary in the transonic dip region. Recent studies have shown that localized contour bumps are particularly effective in increasing the flutter boundary of two-dimensional airfoils under transonic flow conditions [1, 2]. However, convincing evidence for such effects on more realistic swept three-dimensional wings is still lacking.

The natural next step is therefore the experimental investigation of such concepts on realistic swept three-dimensional wings. This, however, requires a dedicated wind-tunnel model exhibiting a well-defined classical flutter mechanism together with a pronounced transonic dip within the operating envelope of the intended wind tunnel. At the DNW Transonic Wind Tunnel Göttingen (DNW-TWG), no such wind-tunnel model was readily available. Although the *Aerostabil* wing was specifically designed for this facility, its flutter behavior is governed by a comparatively unconventional instability mechanism that differs fundamentally from the classical coupled-mode flutter encountered in most practical aircraft configurations [3, 4].

More generally, the availability of experimental benchmark cases for swept three-dimensional wings in transonic flow remains limited. While the AGARD 445.6 wing has become the de-facto standard validation case for transonic flutter prediction, it represents a comparatively thin wing whose transonic dip is located at, or very close to, Mach 1 and therefore only partially reflects the aeroelastic characteristics of modern transport aircraft. Several experimental transonic flutter test cases exist in the literature but, for various reasons, have not become established benchmark configurations. Well-defined benchmark configurations representative of swept transonic wings are therefore highly desirable, both for the validation of advanced aeroelastic prediction methods and for the experimental investigation of novel flutter-suppression concepts.

The present work addresses these challenges through the development of a new swept transonic flutter model for the DNW-TWG. The primary objective was the realization of a wind-tunnel model exhibiting a classical flutter mechanism and a pronounced transonic dip suitable for the experimental investigation of passive and semi-active flutter-suppression concepts. As a by-product, the resulting configuration also provides a new benchmark case for the validation of CFD-based aeroelastic prediction methods.

The paper first formulates the principal design objectives and discusses the resulting aeroelastic design challenges. A hierarchical numerical design workflow combining low- and high-fidelity methods is then presented, followed by a description of the final benchmark configuration. Finally, the aeroelastic behavior of the clean reference wing and the influence of contour bumps are investigated.

2 DESIGN REQUIREMENTS AND CHALLENGES

2.1 Design Objectives

The primary objective of the present work was the development of a swept transonic flutter model for the 1 m $\times$ 1 m test section of the DNW Transonic Wind Tunnel Göttingen (DNW-TWG). Owing to its variable total-pressure capability, the facility permits the dynamic pressure to be varied over a wide range while maintaining an essentially constant Mach number. This provides ideal conditions for determining flutter boundaries by gradually approaching the instability through controlled variations of the dynamic pressure rather than the flight speed.

Within this experimental framework, the wing was required to satisfy several, partly competing, design objectives. First, the flutter mechanism should be governed by the classical interaction of two structural modes, allowing the low-Mach-number behavior to be captured already by Doublet-Lattice aerodynamics. Higher-fidelity CFD methods should become necessary only for the prediction of the transonic flutter behavior, thereby providing a clear separation between classical potential-flow aeroelasticity and additional transonic flow physics.

Second, the wing was required to be rigidly attached to the wind-tunnel sidewall. Since the aeroelastic design studies were intentionally performed without explicitly modelling the wind-tunnel walls, replacing the sidewall by a symmetry boundary condition, the junction flow at the wing root was recognized from the outset as a region of reduced modelling fidelity. To prevent inaccuracies in this numerically challenging flow region from influencing the predicted flutter mechanism, structural motion at the wing root was deliberately minimized.

Third, the wing was required to remain as simple as possible from both a manufacturing and modelling perspective. A shell-based composite construction consisting of an upper and a lower laminate shell with a lightweight foam core was therefore prescribed from the outset. More sophisticated internal load-carrying concepts involving spars or ribs were intentionally excluded, restricting the structural design primarily to the laminate lay-up and the placement of concentrated masses.

Fourth, the model should remain structurally robust enough to permit future investigations not only of flutter but also of higher-angle-of-attack operating conditions approaching flow separation. Consequently, the structural design was governed simultaneously by flutter performance, static strength and manufacturability.

2.2 Aeroelastic Design Challenges

At an early stage of the project, the wing planform was intentionally chosen to remain close to that of the previously investigated Aerostabil wing while increasing the semi-span from 600 mm to 700 mm. Based on this geometric framework, the aerodynamic baseline, comprising the airfoil geometry and the spanwise twist distribution, was established and frozen before the structural pre-design commenced. Rather than pursuing a simultaneous aerodynamic and aeroelastic optimization, the subsequent design effort focused exclusively on realizing the desired flutter characteristics within this prescribed aerodynamic configuration.

The design objectives, together with the prescribed aerodynamic baseline, considerably restricted the available structural design space. Preliminary studies quickly demonstrated that a clean wing satisfying all aerodynamic and structural requirements does not exhibit classical bending-torsion flutter within the attainable dynamic-pressure range of the DNW-TWG. A realistic airfoil thickness together with the prescribed composite shell construction result in a comparatively high torsional stiffness, placing the first torsional frequency well above that of the first bending mode. Simply reducing the structural stiffness was not an option, since the wing simultaneously had to satisfy the prescribed static load requirements.

A straightforward solution would have been to introduce a compliant wing-root attachment in order to reduce the effective torsional stiffness. Since this option had been excluded a priori by the design requirements owing to concerns about the reliable numerical prediction of the motion-induced aerodynamic forces in the wing-wall junction region, an alternative concept was required to achieve classical modal flutter within the prescribed rigid-root configuration.

Instead, an external under-wing pod carrying concentrated masses was introduced to substantially increase the mass moment of inertia and thereby lower the first torsional eigenfrequency. Besides representing a realistic engine-like mass distribution, this concept also enabled the implementation of

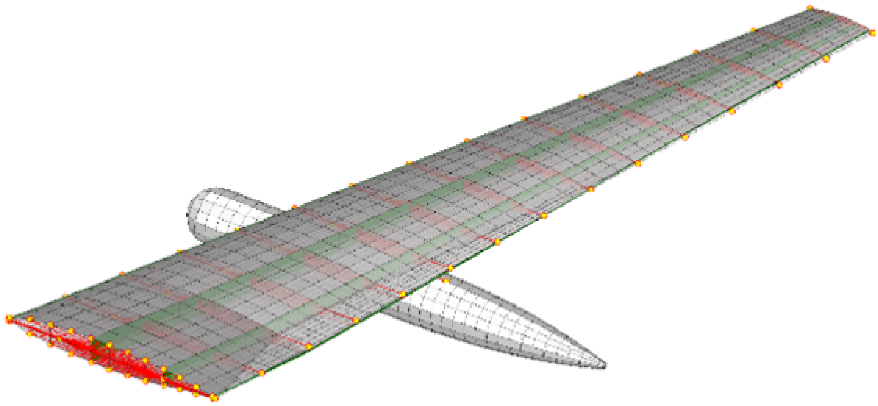

Figure 1: MSC Nastran pre-design finite-element model.

a streamwise-adjustable tuning mass, allowing the flutter boundary to be fine-tuned during the wind-tunnel campaign in order to compensate for unavoidable manufacturing tolerances and uncertainties in the structural damping.

Although the introduction of the under-wing pod substantially reduced the torsional frequency, the preliminary design studies indicated that coupling between the first bending and first torsional modes would still occur only at dynamic pressures well beyond the operating envelope of the DNW-TWG. At the same time, however, the interaction between the *second* bending mode and the first torsional mode emerged as a promising alternative for realizing a classical two-mode flutter mechanism and was therefore investigated further.

3 NUMERICAL DESIGN WORKFLOW

3.1 Low-Fidelity Pre-Design

Following the design objectives outlined in the previous section, the structural pre-design focused on identifying a wing concept capable of exhibiting classical coupled-mode flutter within the operating envelope of the DNW-TWG while simultaneously satisfying the prescribed aerodynamic baseline and structural design constraints. Since numerous structural concepts had to be evaluated during this early design stage, a computationally efficient low-fidelity design environment was employed.

The complete pre-design process was carried out using the DLR in-house parametric modeling framework ModGen [5], which automatically generates a finite-element model for MSC Nastran together with the corresponding Doublet-Lattice aerodynamic model and all required aeroelastic coupling information. This environment enabled rapid manual iteration of the structural concept while continuously assessing both structural integrity and classical flutter behavior.

A resulting finite-element model is shown in **Figure 1**. The composite wing skins are represented by CQUAD4 and CTRIA3 shell elements, whereas the foam core is discretized using CHEXA solid elements. Composite laminate properties are introduced either by equivalent laminate stiffness matrices derived from classical laminate theory or, alternatively, by explicitly modelling the individual ply stacking sequence using standard Nastran composite property definitions (PCOMP/MAT8). A detailed description of the underlying modelling approach is given in [6].

To keep the number of structural design variables manageable, a simplified laminate parameterization was adopted. Instead of optimizing individual plies independently, the laminate was constructed from

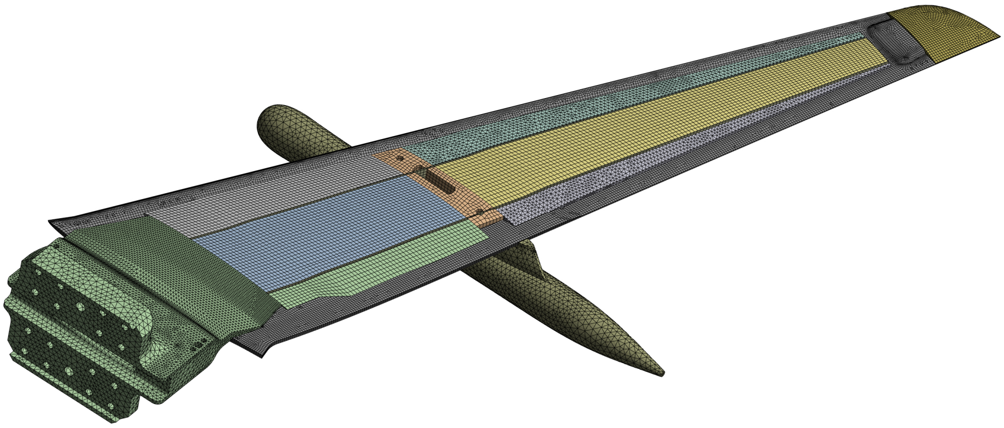

Figure 2: ANSYS high-fidelity structural finite-element model.

a number of predefined symmetric base stacks. Each base stack extends from the wing root to a prescribed spanwise location, resulting in a stepped laminate whose thickness gradually decreases towards the wing tip. In addition, each base stack can be rotated by a prescribed fiber angle, allowing the global bending and torsional stiffness of the wing to be adjusted using only a small number of design parameters.

Within this parameterization, the laminate lay-up was iteratively adjusted to satisfy three objectives simultaneously:

- realization of a DLM-based flutter case within the attainable dynamic-pressure range of the DNW-TWG
- compliance with the prescribed structural load cases
- realization of the target aeroelastic cruise twist distribution defined by the aerodynamic baseline

Unlike a fully automated multidisciplinary optimization, the structural pre-design was therefore performed as an engineering-driven iterative process, combining engineering judgement with repeated structural and aeroelastic analyses. Once a satisfactory flutter mechanism had been identified while simultaneously satisfying the prescribed load requirements and aeroelastic twist distribution, the resulting laminate definition was transferred to the detailed CAD model and served as the basis for the subsequent high-fidelity structural model.

3.2 High-Fidelity Structural Design

The structural concept obtained during the pre-design phase was subsequently transferred into a detailed CAD model developed in CATIA. In contrast to the simplified finite-element representation used during the pre-design stage, the CAD model directly represents the manufacturable wind-tunnel model and therefore served as the master geometry for all subsequent structural analyses and manufacturing activities. Based on the CAD geometry, a high-fidelity finite-element model was generated in ANSYS. Owing to the detailed representation of the composite shell geometry, local thickness variations and geometric details, the resulting structural model contains around 1 million grid points (**Figure 2**).

The primary objective of this design step was the development of a fully manufacturable wind-tunnel model satisfying, in particular, the static strength requirements associated with the anticipated maximum aerodynamic load cases. At the same time, the structural dynamics of the conceptual pre-design

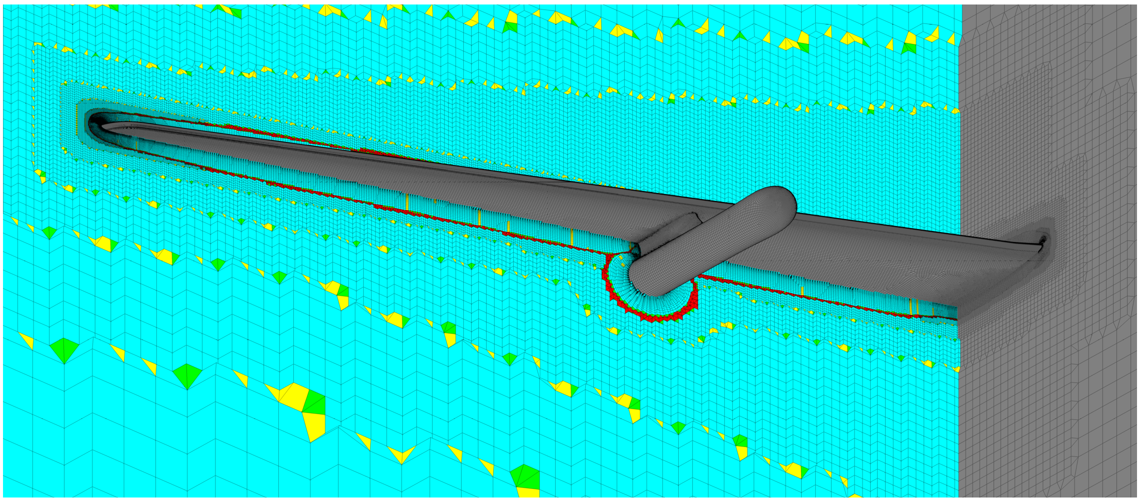

Figure 3: Detail of the RANS mesh with 12.5 million grid points.

had to be reproduced as closely as possible in order to preserve the intended flutter mechanism. Particular emphasis was therefore placed on matching the eigenfrequencies and mode shapes governing the critical modal interaction identified during the pre-design phase. This required several modifications of the structural details, making the preservation of the target modal characteristics an iterative process rather than a direct transfer of the pre-design model. Good agreement between the pre-design and high-fidelity structural dynamics was ultimately achieved. Noticeable differences in the absolute eigenfrequencies remained, whereas the modal characteristics and, in particular, the frequency separation between the critical bending and torsional modes were reproduced with sufficient accuracy for the subsequent CFD-based flutter analyses.

The final structural eigenmodes obtained from the ANSYS model were subsequently interpolated onto the CFD surface mesh and served as the structural basis for all RANS-based aeroelastic analyses presented in the following sections.

3.3 CFD-Based Analysis

The DLM-based flutter analysis described above provides an efficient tool for the structural pre-design and the realization of a classical coupled-mode flutter mechanism. However, the prediction of transonic flutter requires the inclusion of nonlinear flow phenomena beyond the scope of potential-flow aerodynamics. The final aeroelastic assessment was therefore performed using DLR's unstructured RANS solver TAU in combination with the in-house framework *FSForcedMotion*.

The same CFD model that had previously been employed for the aerodynamic baseline design was also used for all aeroelastic analyses. **Figure 3** shows the computational grid, comprising approximately 12.5 million grid points. Turbulence closure is provided by the Spalart-Allmaras model. Consistent with the assumptions adopted during the structural design phase, the wind-tunnel walls were not modeled explicitly. Instead, the tunnel sidewall at the wing root was replaced by a symmetry boundary condition, while the remaining outer boundaries were represented by conventional far-field conditions.

The first 15 structural eigenmodes obtained from the ANSYS model were transferred to the CFD mesh using a dedicated radial basis function interpolation technique and subsequently served as the modal structural basis for all steady and unsteady aeroelastic simulations. Since transonic flutter is expected to depend sensitively on the underlying stationary flow field, all unsteady analyses were performed about a statically coupled aeroelastic equilibrium. This equilibrium was determined beforehand by iteratively coupling the steady RANS solver with the modal structural model.

Starting from this common aeroelastic equilibrium, the aeroelastic stability at a given combination of Mach number Ma and dynamic pressure q is assessed using two complementary approaches:

1. A fully coupled nonlinear fluid-structure interaction (FSI) approach based on the direct time integration of the coupled equations of motion

$$M\ddot{x} + C\dot{x} + Kx = f_A(x, \mathrm{Ma}, q),$$

where M, C and K denote the structural modal mass, damping and stiffness matrices obtained from the finite-element model, x denotes the vector of modal coordinates about the aeroelastic equilibrium, and f_A represents the generalized motion-induced aerodynamic forces. The transient response following a small initial perturbation is subsequently approximated by

$$x(t) \approx \sum_i \hat{x}_i e^{\lambda_i t},$$

using Dynamic Mode Decomposition (DMD). The real part of the identified eigenvalues λ_i represents the modal damping, whereas the imaginary part corresponds to the oscillation frequency [7].

2. A time-linearized approach based on the identification of the matrix-valued aerodynamic influence function $A(\mathrm{Ma}, \omega)$ from the responses of the generalized aerodynamic forces to individual small-disturbance impulse excitation of the structural modes [1, 8]. Once identified, the aerodynamic influence matrix allows the coupled system matrix

$$S(\omega, q, \mathrm{Ma}) = -\omega^2 M + i\omega C + K - \frac{q}{q_A} A(\mathrm{Ma}, \omega)$$

to be assembled for arbitrary values of the dynamic pressure q without requiring additional CFD simulation, since the aerodynamic influence matrix is identified only once at the reference dynamic pressure q_A. Flutter onset is subsequently determined by searching directly for singular system matrices satisfying

$$\det S(\omega, q, \mathrm{Ma}) = 0,$$

which define the neutrally stable operating points forming the flutter boundary. Alternatively, the coupled-system frequency response

$$H(\omega, q) = S^{-1}(\omega, q)$$

is constructed at fixed dynamic pressure and subsequently approximated by means of Vector Fitting [9]. The poles of the resulting rational function approximation (RFA) provide another estimate of the coupled-system eigenvalues.

Throughout the present study, the frequency-domain (FD) formulation serves as the primary engineering tool for determining flutter boundaries owing to its substantially lower computational cost. In contrast to the fully coupled time-domain (TD) simulations, the underlying aeroelastic equilibrium is kept fixed, while the dynamic pressure is varied only virtually through scaling of the aerodynamic influence matrix.

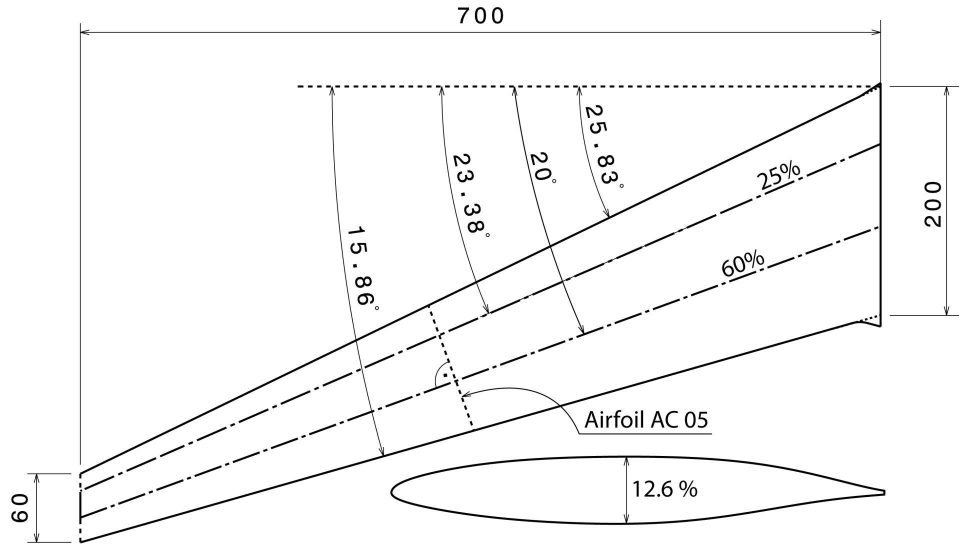

Figure 4: Planform and airfoil definition of the aerodynamic baseline (bottom view).

To assess the accuracy of this approximation, selected operating points are additionally investigated using the fully coupled FSI approach. Modal frequencies and damping ratios are extracted from the resulting transient responses by means of DMD and subsequently compared with the corresponding FD predictions.

4 FINAL BENCHMARK CONFIGURATION

4.1 Aerodynamic Configuration

The aerodynamic definition of the final benchmark configuration is summarized in **Figure 4**. The wing features a trapezoidal planform with a semi-span of 700 mm, a root chord of 200 mm, a tip chord of 60 mm and a taper ratio of 0.3, resulting in an aspect ratio of 10.8. The leading-edge sweep amounts to $25.83°$, corresponding to a sweep angle of $20°$ measured at the 60%-chord line. The resulting mean aerodynamic chord is $c = 0.13\,\mathrm{m}$, and the corresponding reference wing area amounts to $S = 0.091\,\mathrm{m}^2$.

The wing design employs a base airfoil with a relative thickness of 12.6%. Its primary objective was to generate a representative transonic pressure distribution characterized by a pronounced adverse pressure gradient on the upper surface. At the same time, excessive rear loading on the lower surface was deliberately avoided in order to maintain sufficient trailing-edge thickness and thereby suppress undesirable elastic deformation of the trailing edge under aerodynamic loading.

The spanwise twist distribution was determined by steady RANS computations for a representative cruise design point at $Ma = 0.78$ and $c_L \approx 0.5$. Besides establishing the desired spanwise loading, the twist distribution was selected to produce an approximately 2.5-dimensional pressure distribution over large portions of the wing. Furthermore, the local incidence was intentionally reduced in the wing-root region in order to alleviate junction-flow separation at the wind-tunnel sidewall. The resulting steady flow field at the aerodynamic design point is shown in **Figure 5**. As intended, the flow exhibits an extended region of local supersonic flow terminated by a well-defined shock over large portions of the span while remaining predominantly attached.

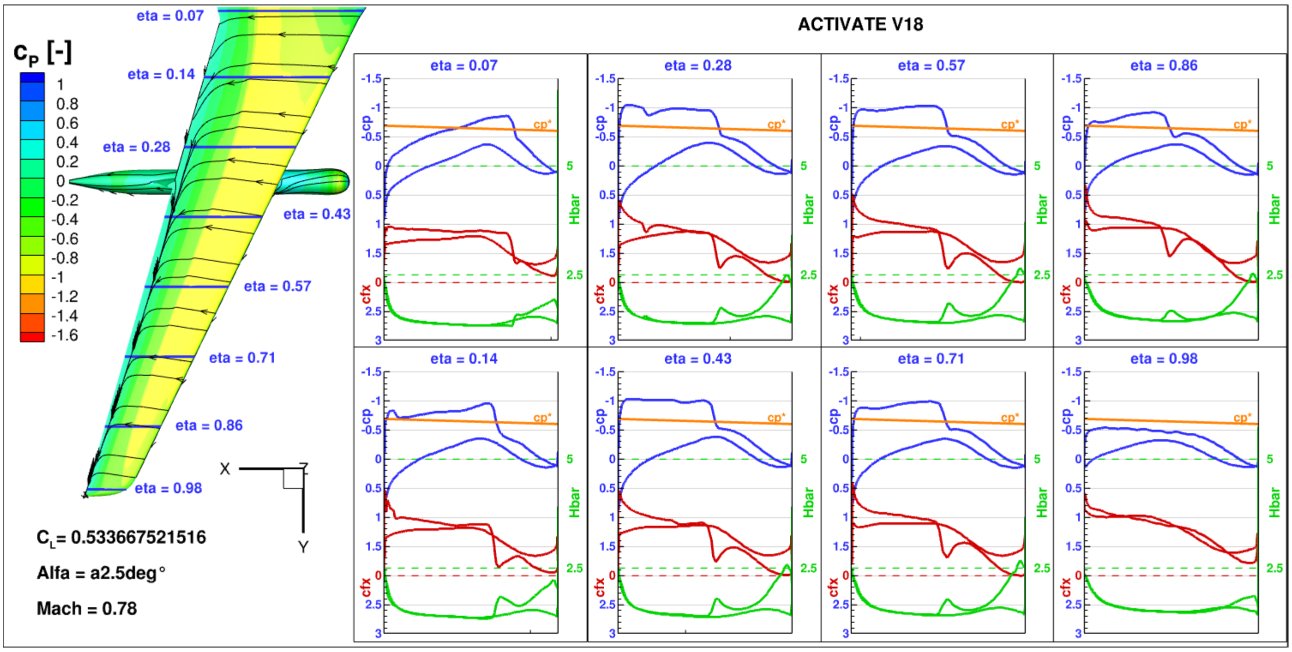

Figure 5: Aerodynamic baseline at the cruise design point $\mathrm{Ma} = 0.78$, $c_L \approx 0.5$.

4.2 Structural Configuration

The final structural configuration of the benchmark wing is shown in **Figure 6**. The model consists of two separately manufactured composite shell halves that are subsequently bonded together to form a closed load-carrying shell. No internal spar or rib structure is employed. Instead, the required global stiffness is provided almost entirely by the composite laminate in combination with the closed shell geometry. A lightweight foam core is incorporated to stabilize the thin composite skins against local buckling and therefore contributes only marginally to the overall structural stiffness.

An external pod attached beneath the wing accommodates a movable 200 g tungsten tuning mass. By adjusting its streamwise position, moderate deviations of the flutter boundary arising from manufacturing tolerances and uncertainties in the structural damping can be compensated without modifying either the aerodynamic outer mold line or the structural layout of the wing. Furthermore, the nose cap of the pod was designed as an interchangeable component, allowing the pod inertia to be adapted, if required, by replacing the aluminum cap with an equivalent steel component. A second partly interchangeable tuning mass of 150 g is integrated into the wing tip.

The laminate definition transferred from the structural optimization into the CAD model is summarized in **Figure 7**. Both wing shells are manufactured from a unidirectional (UD) E-glass fabric with a dry areal weight of $220\,\mathrm{g/m^2}$ and a fiber distribution of 93% in the warp direction and 7% in the weft direction. Based on previous experience regarding both material properties and processability, E-Glass Silenka fibers with an elastic modulus of 74 GPa were selected. The resulting laminate was subsequently used consistently throughout all numerical analyses and for the manufacturing of the wind-tunnel model.

4.3 Structural Dynamic Characteristics

The first three eigenfrequencies of the final benchmark configuration are shown in **Figure 8** for the four pod-mass configurations considered throughout the present study. The movable tuning mass primarily affects the first torsional mode. While the first and second bending frequencies remain

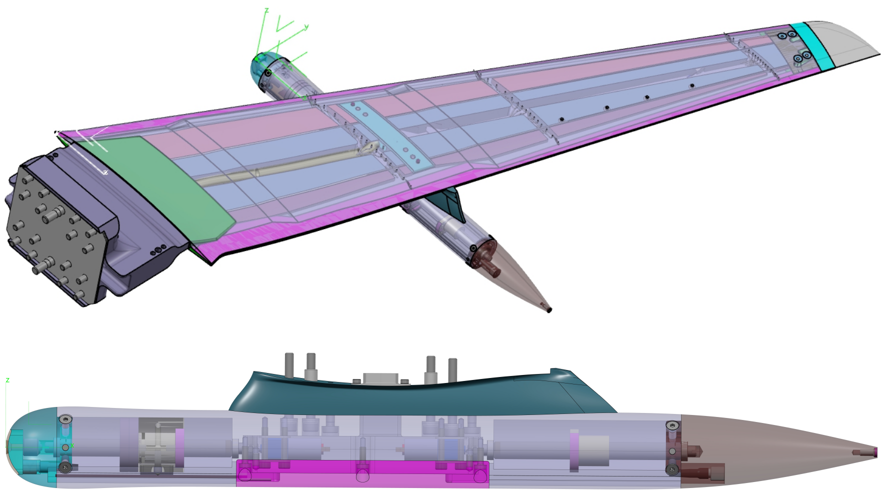

Figure 6: Final CAD model of the benchmark wing.

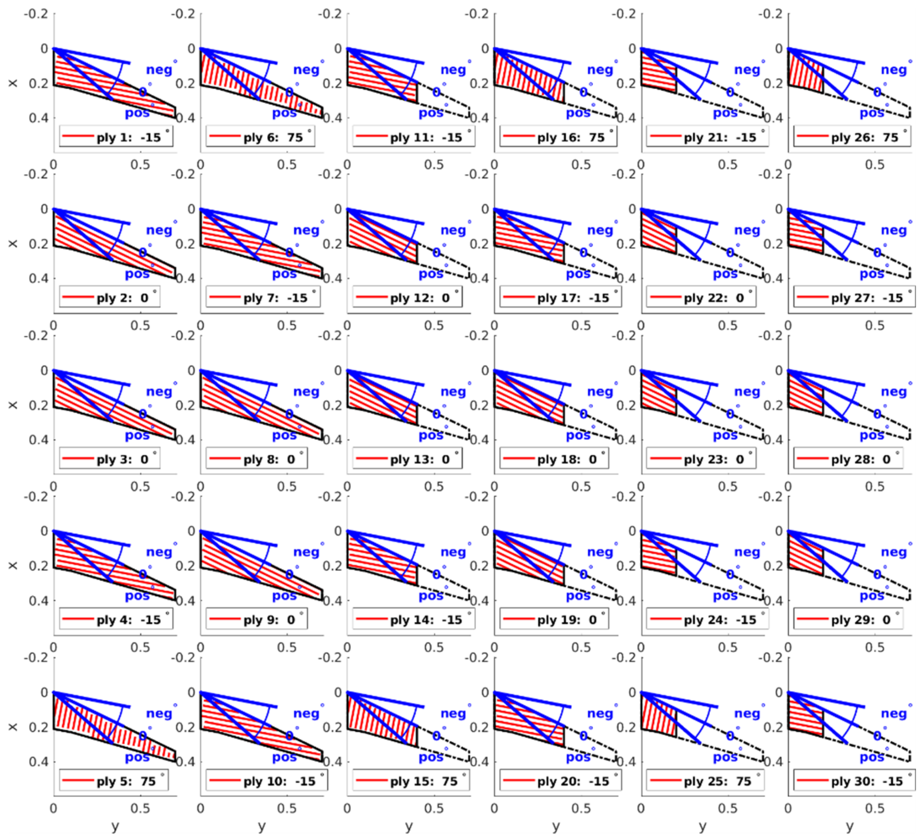

Figure 7: Ply book containing the optimized laminate definitions resulting from the pre-design.

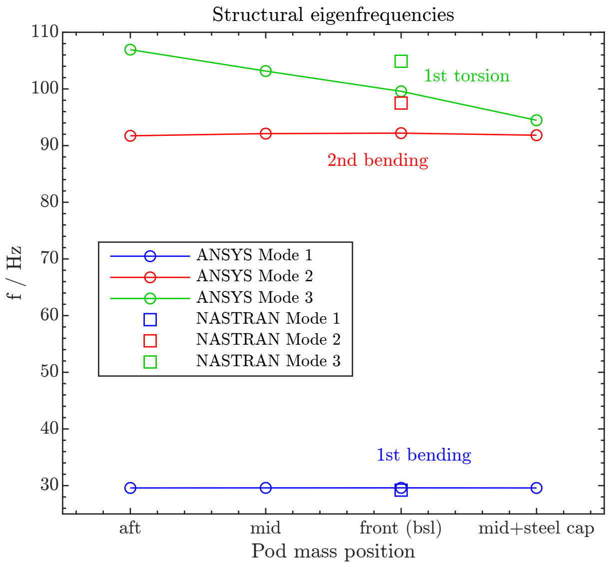

Figure 8: Effect of pod mass position on the evolution of first three structural eigenfrequencies.

nearly unchanged, the first torsional frequency decreases continuously as the tuning mass is shifted towards the pod nose. Consequently, the frequency separation between the second bending mode and the first torsional mode can be adjusted over a comparatively wide range without significantly modifying the remaining structural dynamics. Further shown is a comparison of the eigenfrequencies of the final high-fidelity ANSYS model with those obtained from the conceptual MSC Nastran pre-design model for the baseline pod mass configuration. Although differences remain in the absolute eigenfrequencies, the frequency separation between the second bending and first torsional mode is reproduced remarkably well.

The corresponding mode shapes are presented in **Figure 9**. Their overall characteristics remain nearly unchanged for all investigated pod mass configurations, indicating that the tuning concept predominantly affects the modal frequencies while preserving the global deformation patterns. The second bending mode (Mode 2) already exhibits a noticeable torsional component over the midboard wing region, while the outboard wing retains the characteristic deformation pattern of a bending mode. The corresponding nodal line extends continuously from the wing tip towards the nose of the under-wing pod, resulting in a pronounced rotation of the pod about its nose, where the movable tuning mass is located. In contrast, the first torsional mode (Mode 3) is characterized by substantial rotation of the complete wing and under-wing pod. As the tuning mass is shifted towards the pod nose, the apparent torsional axis gradually moves aft, reflecting the accompanying modification of the modal deformation pattern.

5 RESULTS

5.1 Clean-Wing Flutter Behavior

The aeroelastic response of the benchmark wing is first investigated using the frequency-domain formulation introduced in Section 3. The numerically predicted flutter boundaries of the final reference configuration are summarized in **Figure 10**. The graph compares the flutter boundaries in terms of the critical (incompressible) dynamic pressure $q = \rho_\infty V^2/2$ as obtained from the conceptual DLM-based pre-design model (NASTRAN+DLM) with those computed using the high-fidelity CFD-based frequency-domain approach (ANSYS+RANS). The operating envelope of the TWG in terms of the total (stagnation) pressure p_0 and the flutter boundary obtained with the Aerostabil wing

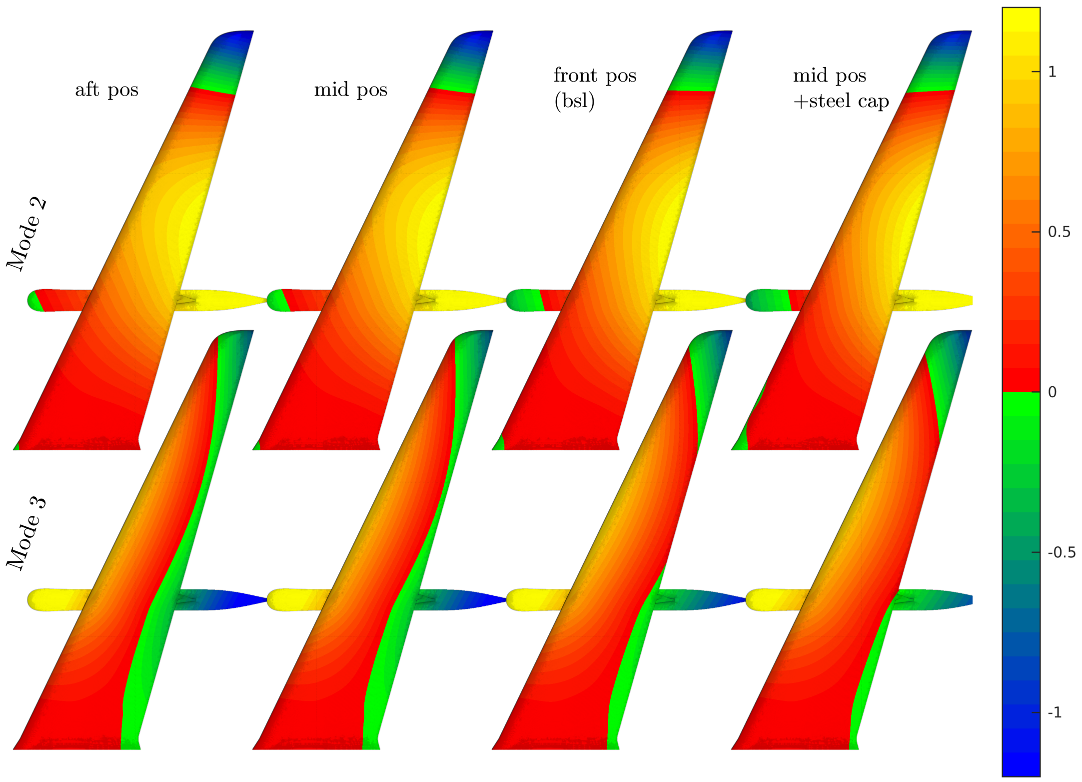

Figure 9: Effect of pod mass position on the modeshapes of the second bending and first torsional modes (out-of-plane component of the ANSYS modes projected onto the CFD surface mesh).

in 2003 are given for reference. At low Mach numbers, both approaches predict nearly identical flutter boundaries. This confirms that the intended flutter mechanism is already captured by classical potential-flow aeroelasticity. A fundamentally different behavior emerges in the transonic regime. While the DLM solution predicts the expected monotonic decrease of the flutter boundary with increasing Mach number, the CFD-based analysis exhibits a pronounced transonic dip followed by a rapid recovery at higher Mach numbers. The resulting minimum lies entirely within the attainable operating range of the DNW-TWG. Although the two structural models exhibit small differences, the observed discrepancies in the predicted flutter boundary can largely be attributed to the aerodynamic modelling. This conclusion is supported by additional computations (not shown here), in which the modal basis of the MSC Nastran pre-design model was coupled with the high-fidelity CFD solver. These Nastran+RANS calculations produced virtually the same flutter boundary as the corresponding ANSYS+RANS simulations.

To verify the flutter boundary shown in Figure 10, fully coupled FSI simulations were performed at discrete dynamic pressure levels for a constant Mach number of $Ma = 0.75$, close to the minimum of the transonic dip. **Figure 11** presents the resulting time histories of the first three generalized modal coordinates. For the two lower dynamic pressures, all structural oscillations decay with time, indicating a stable aeroelastic system. In contrast, the two higher dynamic pressures exhibit exponentially growing oscillations, demonstrating the onset of flutter. It is further evident that the observed flutter instability beyond the critical dynamic pressure is dominated by the interaction of Modes 2 and 3, whereas the low-frequency oscillations associated with the first bending mode remain damped throughout all investigated dynamic pressure levels.

The transient responses shown in Figure 11, together with additional simulations performed at higher dynamic pressures, were subsequently analyzed using Dynamic Mode Decomposition (DMD) in or-

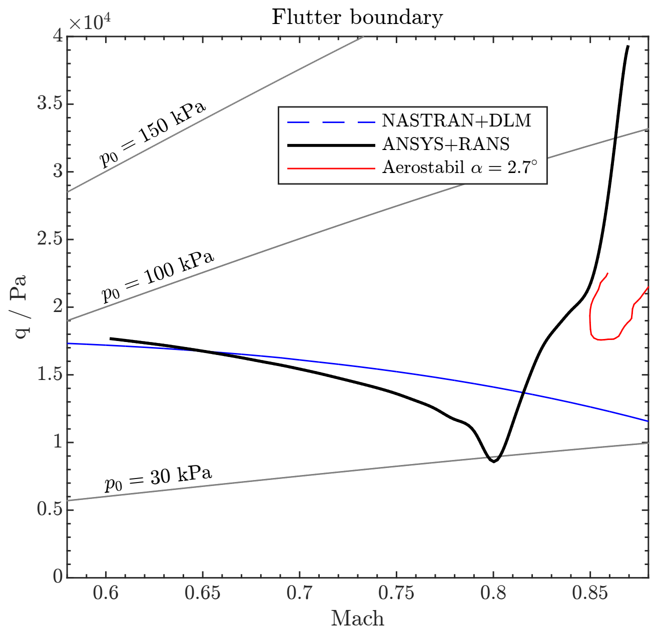

Figure 10: Comparison of predicted flutter boundaries of the reference configuration obtained from low- and high-fidelity aeroelastic analyses.

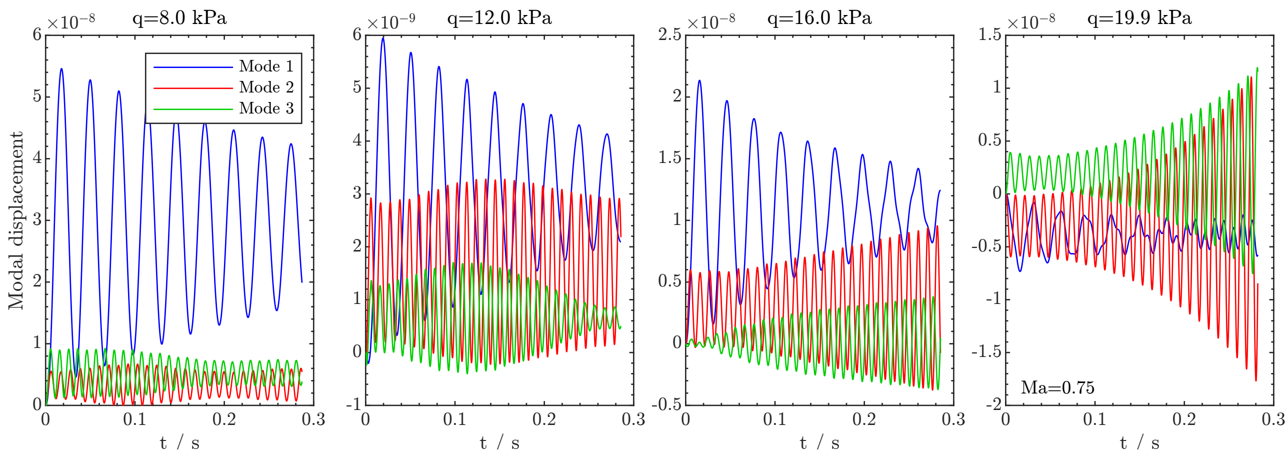

Figure 11: Fluid-structure coupled time-domain simulations of the baseline pod mass configuration at four different dynamic pressures below and beyond the flutter boundary at $\mathrm{Ma} = 0.75$

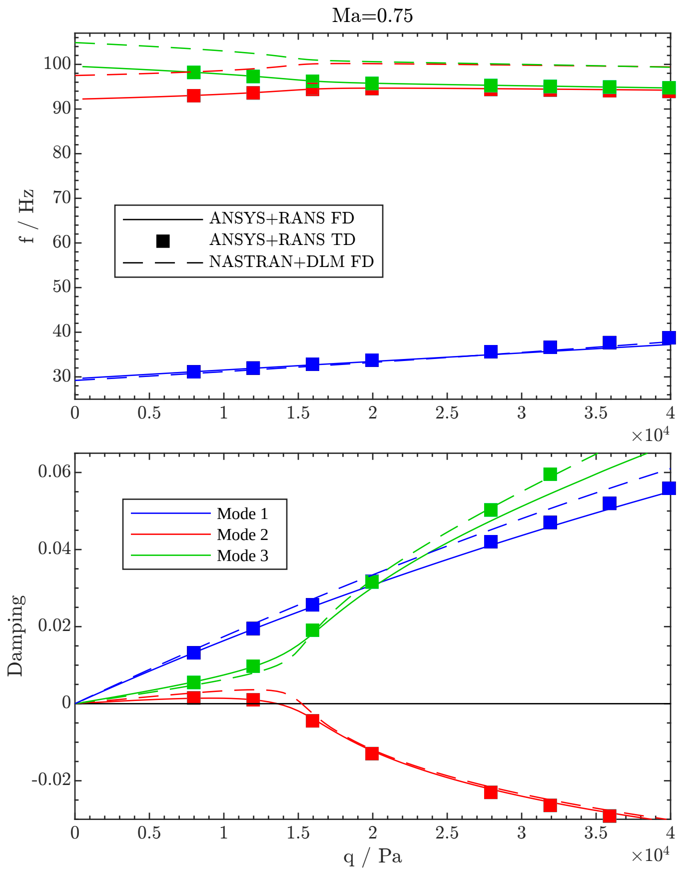

Figure 12: Comparison of CFD-based frequency-domain (FD) and fluid-structure coupled time-domain (TD) results at $\mathrm{Ma} = 0.75$ including corresponding DLM-based flutter analysis for reference.

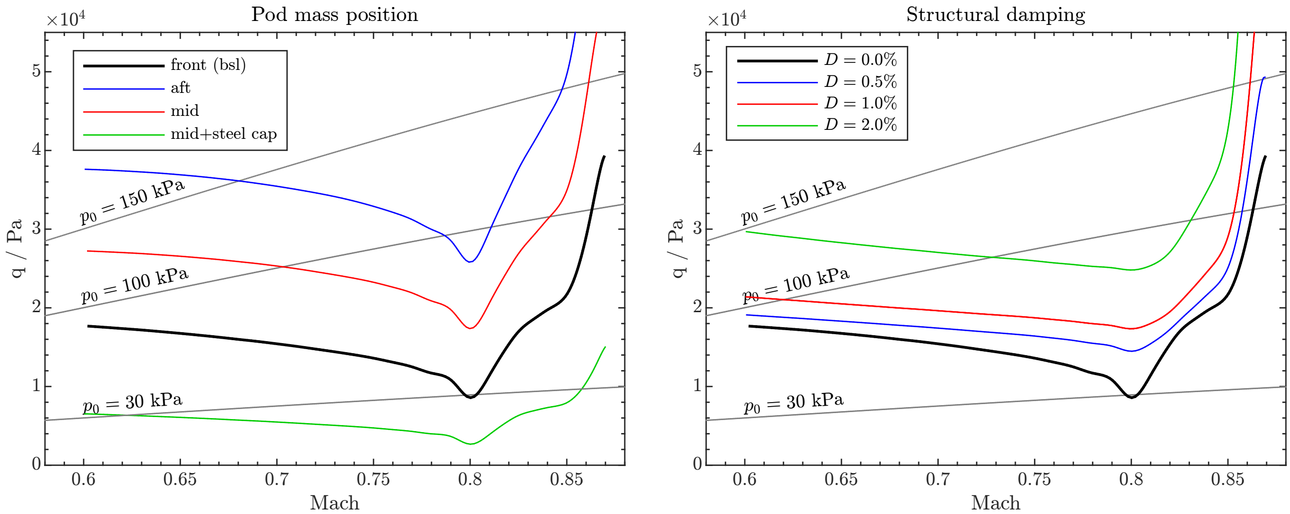

Figure 13: Effect of pod tuning mass location and hypothetical structural modal damping

der to extract the modal frequencies and damping ratios. The resulting estimates are compared with the corresponding frequency-domain predictions in **Figure 12**. While Figure 10 only shows the flutter boundary, corresponding to the very dynamic pressure at which one aeroelastic mode becomes neutrally stable, Figure 12 presents the complete evolution of the corresponding complex eigenvalues with increasing dynamic pressure. Excellent agreement is obtained over the entire investigated range of dynamic pressures between the frequency-domain (FD) and the selective time-domain (TD) results. Small discrepancies can be observed for the more heavily damped modes. This behavior is expected, since both the frequency-domain approach based on Vector Fitting and the time-domain analysis using DMD rely on approximate rather than exact eigenvalue identification techniques.

Further, Figure 12 also includes the results of the low-fidelity MSC Nastran SOL 145 flutter analysis based on the pre-design model (dashed lines). At zero dynamic pressure, the previously discussed frequency offset between pre-design model and the high-fidelity ANSYS model is clearly visible for the second and third structural modes (see Figure 8). Despite these differences in the initial eigenfrequencies, the subsequent evolution of the aeroelastic eigenvalues with increasing dynamic pressure is qualitatively identical. Both the DLM-based and the CFD-based aerodynamic models predict the same underlying flutter mechanism, namely the coupling between the second bending mode and the first torsional mode promoted by their progressively decreasing frequency separation.

A key feature of the present wind-tunnel model is the streamwise adjustable tuning mass located in the forward section of the under-wing pod. The left-hand side of **Figure 13** illustrates its influence on the predicted flutter boundary. Moving the tuning mass aft shifts the flutter boundary almost uniformly towards higher dynamic pressures, whereas a forward displacement lowers the flutter boundary accordingly. Replacing the aluminum nose cap of the pod by an equivalent steel component produces an additional forward shift of the overall center of gravity and results in a further reduction of the flutter boundary. Remarkably, these structural modifications leave the characteristic shape of the transonic dip largely unchanged, indicating that the tuning concept primarily shifts the overall flutter level without altering the underlying aeroelastic mechanism.

The observed influence of the pod tuning mass is fully consistent with its previously introduced effect on the structural dynamics (see Figure 8 and 9). Shifting the mass towards the pod nose reduces the frequency separation between the two critical modes while simultaneously causing a downstream displacement of the nodal line of the first torsional mode (Mode 3). At present, it is not possible

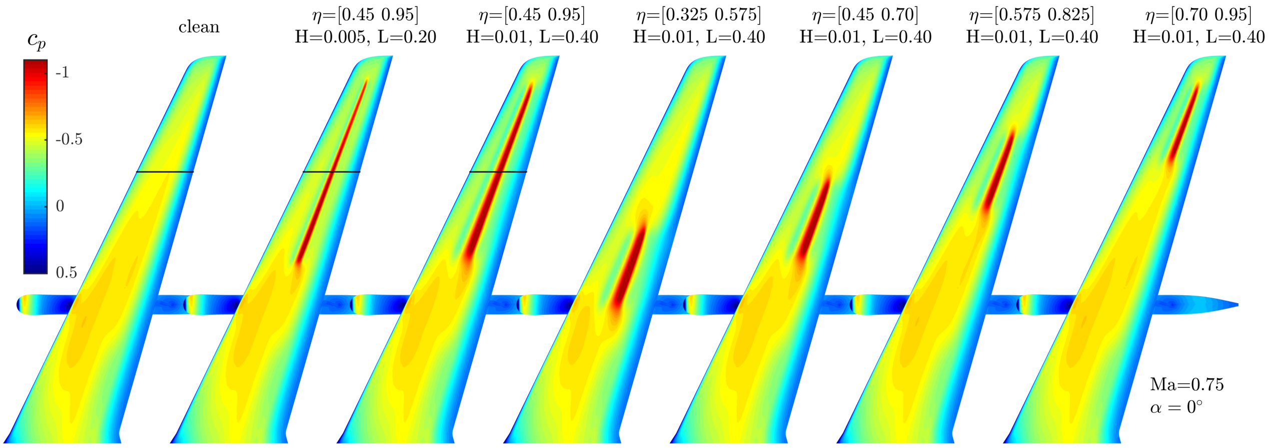

Figure 14: Influence of contour bumps on the steady surface pressure field (H: bump height relative to local chord, L: chordwise length relative to local chord).

to unambiguously distinguish the relative contributions of these two effects to the observed flutter behavior.

In all flutter analyses presented so far, both in the time and frequency domains, the structural damping was assumed to be zero. This represents the conventional and conservative assumption adopted in many numerical flutter studies. In the actual wind-tunnel model, however, structural damping is inevitably present. The right-hand panel in **Figure 13** illustrates the influence of assumed structural damping levels on the flutter boundary of the baseline pod mass configuration. The modal damping matrix was assumed as $C = 2D\sqrt{K}$, such that all structural modes exhibit identical modal damping ratios. As expected, increasing structural damping shifts the flutter boundary towards higher dynamic pressures. The increase, however, is not strictly proportional to the assumed damping level. Furthermore, structural damping tends to smooth the characteristic shape of the transonic dip, resulting in a less pronounced minimum of the flutter boundary.

5.2 Effect of Contour Bumps on Flutter

Before discussing the influence of contour bumps on the unsteady aeroelastic behavior, their influence on the underlying steady flow field is first examined. **Figure 14** compares the clean-wing pressure distribution at $\mathrm{Ma} = 0.75$ and $\alpha = 0°$ with six representative contour-bump configurations. In all cases, the bump is positioned at the mid-chord location, $\xi_c = 0.50$. It is immediately apparent that all bump geometries locally accelerate the flow, giving rise to a pronounced low-pressure region that is clearly visible as the red spots in the surface pressure coefficient distribution, c_p. Complementing the surface pressure distributions in Figure 14, the right-hand panel of **Figure 15** presents corresponding spanwise pressure sections at $\eta = 0.70$ for the three left-most configurations depicted in Figure 14 (indicated by the black line), again at $\mathrm{Ma} = 0.75$ and $\alpha = 0°$. In addition, a configuration with an identical contour bump located on the *lower* wing surface is included (not shown in Figure 14). All bump configurations accelerate the local flow sufficiently to produce a region of supersonic flow, as indicated by the pressure coefficient falling below the Mach-specific critical isentropic value, c_p^*. The aerodynamic impact is qualitatively very similar for bumps located on the upper and lower wing surfaces while the larger bump naturally produces a stronger acceleration than the smaller, lower-profile configuration. A particularly noteworthy observation is that the clean-wing pressure distribution at this spanwise location remains entirely subsonic. The local transonic flow region is generated exclusively by the contour bump. For comparison, the left-hand panel in Figure 15 shows the corre-

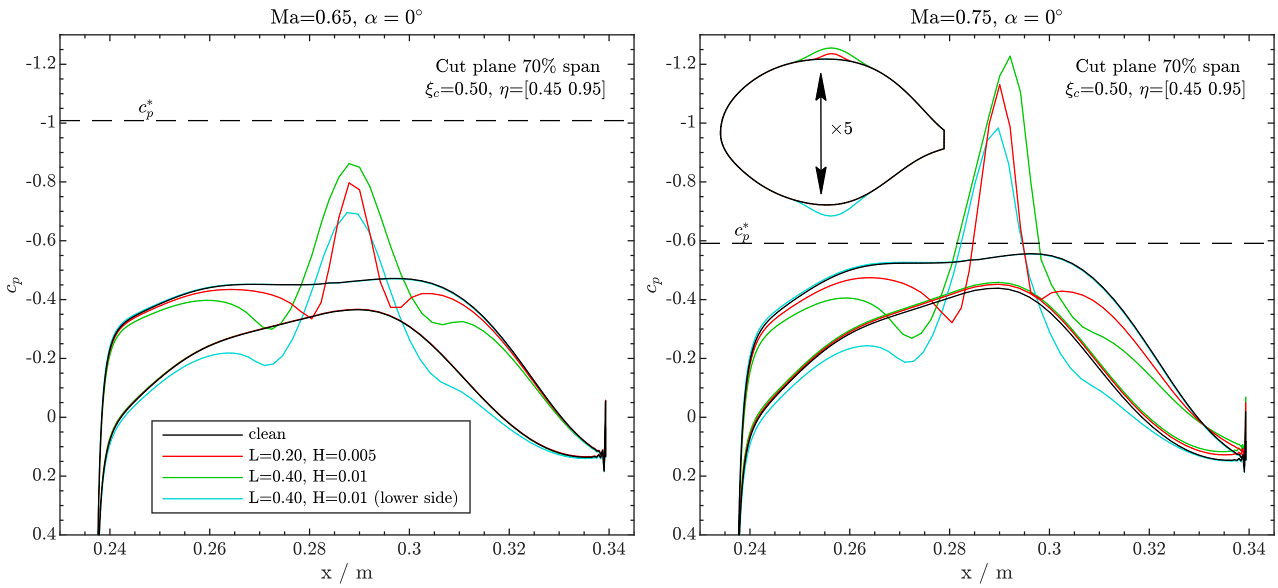

Figure 15: Pressure sections at 70% half-span. Left: subsonic flow; right: transonic flow.

sponding pressure distributions for the same contour-bump configurations at the lower Mach number of $\mathrm{Ma} = 0.65$. Qualitatively, the aerodynamic response is very similar. All bump geometries produce the characteristic local suction peak associated with the acceleration of the flow over the bump. In contrast to the transonic case at $\mathrm{Ma} = 0.75$, however, the local flow remains entirely subsonic, and the pressure coefficient nowhere falls below the critical isentropic value, c_p^*.

For the sake of completeness, it should be noted that some of the larger bump geometries ($H = 0.01$) produce small shock-induced separation regions in the steady RANS solution at $\mathrm{Ma} = 0.75$ (see Figure 14). These separated regions typically extend over only a few percent of the local chord before the boundary layer reattaches. For the smaller contour bump ($H = 0.005$, $L = 0.20$), no such separation is observed. In the present study, these localized separation bubbles are regarded as a secondary effect. Based on the evidence presented below, we do not consider shock-induced boundary-layer separation to be the primary mechanism responsible for the observed changes in flutter behavior.

Figure 16 summarizes the influence of various contour-bump configurations on the flutter boundary of the baseline pod mass configuration at an angle of attack of $\alpha = 0°$. The left-hand panel investigates the effect of the chordwise bump position for constant bump dimensions, whereas the right-hand panel compares two bumps of different size. Among the chordwise positions considered, the configuration centered at $\xi_c = 0.50$ produces the largest increase in the flutter boundary. Shifting the bump further upstream to $\xi_c = 0.40$ and $\xi_c = 0.30$ progressively reduces its effectiveness and even leads to a slight deterioration of the flutter boundary through a forward shift of the transonic-dip minimum. The size variation shown in the right-hand panel demonstrates that the influence on the flutter boundary generally increases with bump height and streamwise extent. However, the relationship is clearly nonlinear, indicating that the aerodynamic response cannot be explained by bump dimensions alone.

A striking observation is that the flutter boundary remains almost unaffected throughout the subsonic regime for $\mathrm{Ma} < 0.70$. This indicates that the substantial modifications of the steady pressure distribution produced by the contour bumps under purely subsonic conditions (cf. Figure 15 for $\mathrm{Ma} = 0.65$) have little influence on the motion-induced unsteady aerodynamic forces governing the flutter behavior. In contrast, the contour bumps become effective only once local transonic flow regions are

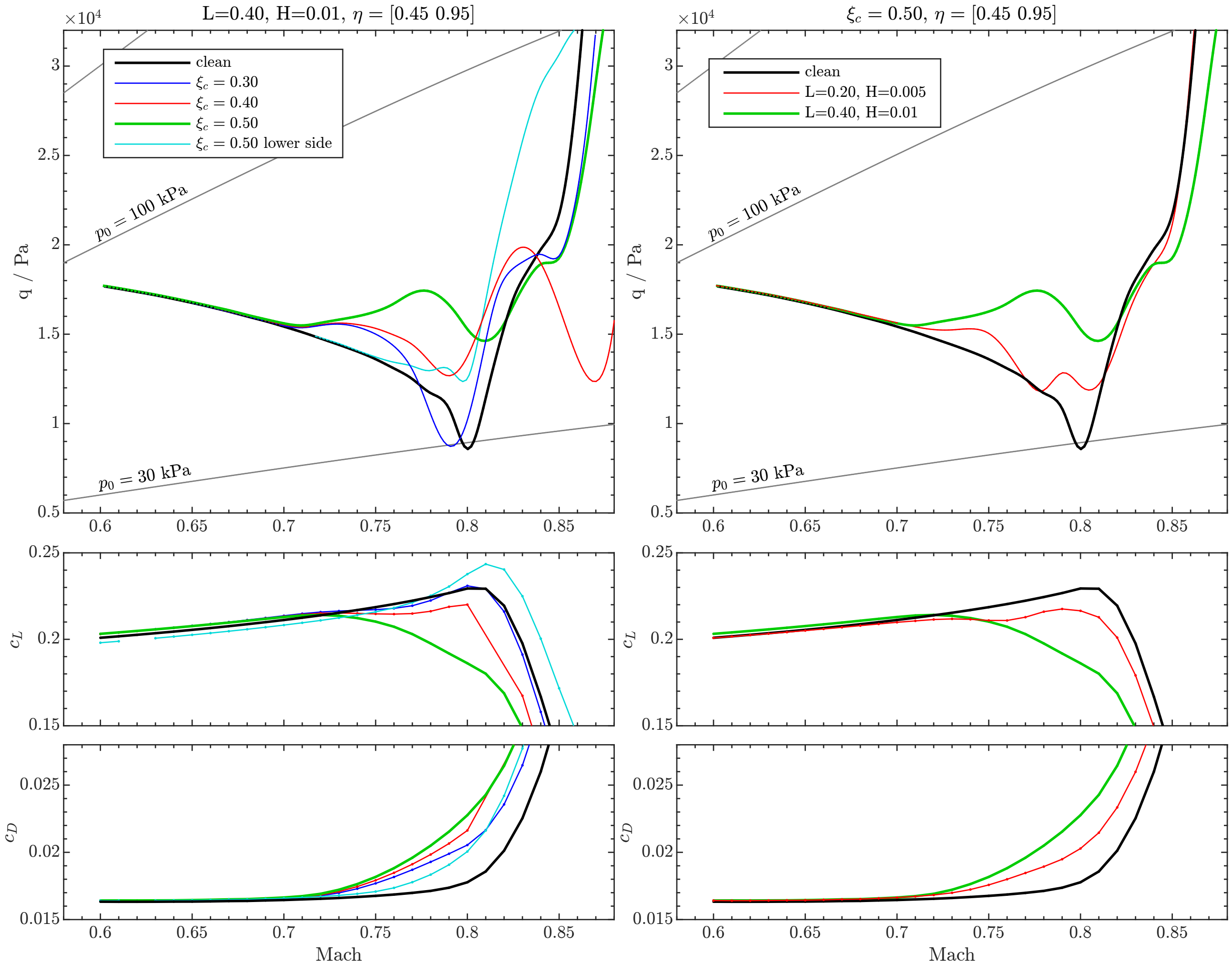

Figure 16: Influence of various contour-bump configurations on the flutter boundary of the baseline pod mass configuration.

present, or when they induce such regions themselves. From an aeroelastic point of view, the bumps are therefore essentially transparent in purely subsonic flow. This interpretation is further supported by the corresponding steady lift and drag coefficients of the aeroelastic equilibrium also shown in Figure 16. Throughout the purely subsonic regime, the contour bumps have only a negligible influence on the steady aerodynamic coefficients. Pronounced changes occur only once transonic flow effects become significant. At the constant angle of attack of $\alpha = 0°$, the bumps produce a noticeable reduction in lift accompanied by a distinct increase in drag. This drag rise corresponds closely to the increase observed for the clean wing only at considerably higher Mach numbers and therefore provides a clear indication that the contour bumps induce local supersonic flow regions.

It should be emphasized that the present study represents an initial investigation of contour-bump effects on the newly developed benchmark wing rather than a systematic optimization. From a purely aerodynamic point of view, the flutter analyses would ideally be performed at constant lift rather than at constant angle of attack. This, however, would require an additional trim loop during the computation of each statically coupled aeroelastic equilibrium. More importantly, the numerical setup adopted here closely reflects the intended wind-tunnel procedure. The initial experimental campaign will likewise determine the flutter boundary at fixed angles of attack. The associated changes in lift introduced by the contour bumps are therefore deliberately accepted rather than eliminated by a trim procedure. Conducting the measurements at constant lift would require a sufficiently accurate force balance together with an active adjustment of the angle of attack throughout the test. Such a setup would be difficult to reconcile with the very stiff wing-root attachment required for the present benchmark configuration.

So far, only contour bumps with a comparatively large spanwise extent, covering the region $\eta = [0.40\ 0.95]$, have been considered. The following investigation therefore focuses on shorter bump geometries extending over only 25% of the semi-span (see the four configurations on the right in Figure 14), which are additionally shifted to different spanwise positions. **Figure 17** compares the corresponding flutter boundaries with those obtained for the long reference bump located at $\xi_c = 0.50$. It can be seen that the shorter bumps positioned in the inboard and mid-span regions already reproduce most of the beneficial effect of the baseline bump configuration. In contrast, bumps placed near the wing tip have almost no influence on the flutter boundary, despite producing pronounced local supersonic flow regions comparable to those generated by the more effective configurations (as indicated by the transonic drag rise). The observed spanwise dependence suggests that the effectiveness of the contour bumps is closely related to the structural mode shapes underlying the flutter mechanism. In the present benchmark configuration, both the second bending mode and the first torsional mode exhibit their largest vibration amplitudes over the mid-span region (see Figure 9). This is precisely where the most effective bump configurations are located. In contrast, the outboard wing contributes comparatively little to the energy transfer during flutter, implying that only limited energy exchange between the structure and the surrounding flow can take place in this region. Consequently, modifying the local flow field near the wing tip can be expected to have only a minor influence on the flutter behavior.

The results presented so far demonstrate that contour bumps can significantly modify the flutter boundary in the vicinity of the transonic dip. Since the bumps are introduced exclusively as geometric modifications of the aerodynamic surface, they have, by definition, no influence on the structural dynamic properties of the benchmark wing. The observed changes in flutter behavior must therefore originate entirely from modifications of the aerodynamic forces acting on the vibrating structure. Within the present frequency-domain formulation, these aerodynamic forces are represented by the complex aerodynamic influence matrix $A(\mathrm{Ma}, \omega)$. **Figure 18** compares the four aerodynamic matrix

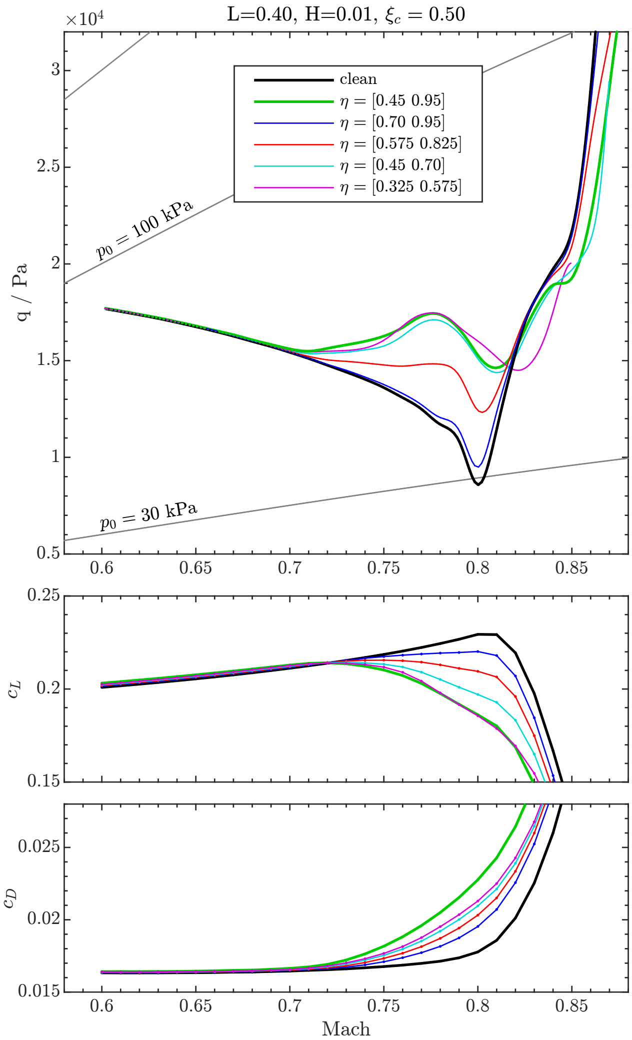

Figure 17: Effect of spanwise bump location and extension

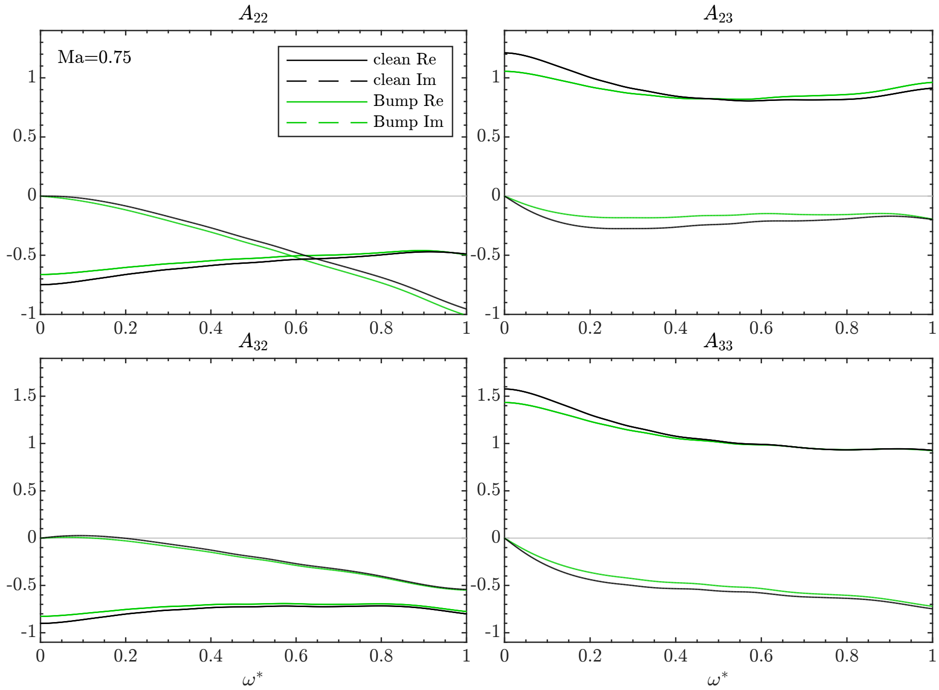

Figure 18: Aerodynamic influence matrix of the participating flutter modes at $\mathrm{Ma} = 0.75$ for the baseline clean configuration and the baseline bump configuration.

elements associated with the participating flutter modes for the clean configuration and the baseline bump geometry ($\eta = [0.45\ 0.95]$, $H = 0.01$, $L = 0.20$), once more at $\mathrm{Ma} = 0.75$. Small but systematic differences between the clean and bump configurations can be observed in all four elements of the aerodynamic influence matrix. For the present flutter case, particular attention should therefore be paid to the reduced frequency $\omega^* \approx 0.3$, at which the flutter instability occurs. Although the modifications of the individual matrix elements appear comparatively small, they are evidently sufficient to produce the pronounced changes in the flutter boundary discussed above. At present, however, it is not possible to attribute the observed stabilization effect to any single matrix component. Rather, it appears to result from the combined influence of subtle changes distributed throughout the aerodynamic influence matrix.

A closer inspection of Figure 18 reveals that noticeable differences between the clean and bump configurations already exist in the limit of zero reduced frequency. This observation motivates a second comparison in which the quasi-steady aerodynamic derivatives are evaluated over the complete Mach-number range at $\omega^* = 0$. The resulting Mach-number dependence is shown in **Figure 19**. Remarkably, the evolution of the quasi-steady aerodynamic derivatives closely resembles the corresponding changes observed in the flutter boundary. In particular, the largest differences between the clean and bump configurations occur precisely in the Mach-number range where the transonic dip is most pronounced, whereas only minor differences are found in the purely subsonic regime.

Although the present observations do not establish a rigorous causal relationship, they strongly suggest that the dominant bump effect is already contained in the quasi-steady aerodynamic derivatives. The frequency dependence of the aerodynamic matrix appears to provide only a secondary correction for the present benchmark configuration.

This finding is particularly encouraging from an engineering perspective. If the dominant influence of contour bumps is indeed contained already in the quasi-steady aerodynamic derivatives, preliminary bump designs may no longer require repeated unsteady flutter analyses. Instead, stationary RANS

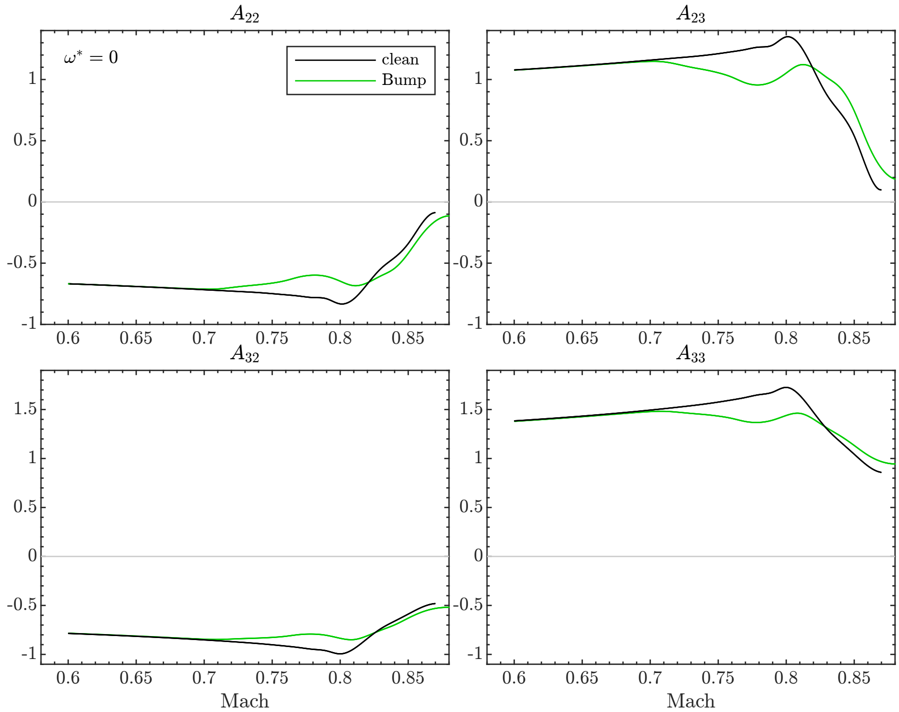

Figure 19: Quasi-steady aerodynamic influence matrix of the participating flutter modes for the baseline clean configuration and the baseline bump configuration.

calculations could provide valuable guidance during the early design stages, while the more expensive frequency-domain flutter analysis would be reserved for the final verification of promising candidate geometries.

6 CONCLUSIONS

In the present work, a new transonic aeroelastic benchmark wing for the DNW-TWG has been developed. The design combines a classical coupled-mode flutter mechanism with a pronounced transonic dip while satisfying the geometric and structural constraints imposed by the wind-tunnel environment. A hierarchical design workflow combining low-fidelity DLM-based structural pre-design with high-fidelity CFD-based aeroelastic analyses proved capable of realizing the desired flutter characteristics. Good agreement between nonlinear FSI simulations and the linearized frequency-domain formulation was obtained over the investigated operating range, supporting the use of the latter as an efficient engineering tool. The first numerical investigation of contour-bump effects on the new benchmark demonstrated that comparatively small geometric modifications can substantially increase the flutter boundary in the vicinity of the transonic dip while leaving the low-Mach-number behavior largely unaffected. The results further suggest that the dominant mechanism is already contained in the quasi-steady aerodynamic derivatives, indicating that stationary CFD computations may provide valuable guidance during future bump-design studies. The next step of the project will be the manufacturing and experimental investigation of the benchmark model in the DNW-TWG with the first experimental campaign being scheduled for early 2027. Besides providing the first experimental validation of contour-bump-based flutter suppression, the resulting data set is expected to constitute a valuable reference case for the validation of future CFD-based aeroelastic prediction methods.

ACKNOWLEDGEMENTS

Parts of the research leading to this work have received funding from the the German Federal Ministry of Economic Affairs and Energy (BMWE) in the framework of the Federal Aeronautical Research Program (LuFo) VII-1 within the project SaFuMa (FKZ: 20E2409F).

7 REFERENCES

[1] Nitzsche, J., Otte, J., Kaiser, C., et al. (2022). The Effect of Shock Control Bumps on the Transonic Flutter and Buffeting Characteristics of a Typical Wing Section. In *Proc. of the 19th International Forum on Aeroelasticity and Structural Dynamics (IFASD), Madrid, Spain, 13-17 June 2022*.

[2] Altkuckatz, A., Braune, M., Dillinger, J., et al. (2024). Experimental Investigation of Shock Control Bumbs on the Transonic Dip of the OAT15A Airfoil. In *Proc. of the 20th International Forum on Aeroelasticity and Structural Dynamics (IFASD), The Hague, Netherlands, 17-21 June 2024*.

[3] Stickan, B., Dillinger, J., and Schewe, G. (2014). Computational aeroelastic investigation of a transonic limit-cycle-oscillation experiment at a transport aircraft wing model. *Journal of Fluids and Structures*, 49, 223–241. ISSN 0889-9746. doi: https://doi.org/10.1016/j.jfluidstructs.2014.04.014.

[4] Schewe, G. and Mai, H. (2019). Experiments on transonic limit-cycle-flutter of a flexible swept wing. *Journal of Fluids and Structures*, 84, 153 – 170. doi:10.1016/j.jfluidstructs.2018.07.005. Cited by: 8.

[5] Klimmek, T. (2009). Parameterization of topology and geometry for the multidisciplinary optimization of wing structures. In *Proceedings of the European Air and Space Conference (CEAS 2009)*. Manchester, UK.

[6] Dillinger, J., Meddaikar, M. Y., Lübker, J., et al. (2019). Design and optimization of an aeroservoelastic wind tunnel model. Paper IFASD-2019-078. In *Proc. of the 18th International Forum on Aeroelasticity and Structural Dynamics (IFASD), Savannah, GA, USA, 9-13 June 2019*.

[7] Ibrahim, S. and Mikulcik, E. (1977). A method for the direct identification of vibration parameter from the free response. *Shock and Vibration Bulletin*, 47, 183–198.

[8] Nitzsche, J., Ringel, L. M., Kaiser, C., et al. (2019). Fluid-mode flutter in plane transonic flows. Paper IFASD-2019-006. In *Proc. of the 18th International Forum on Aeroelasticity and Structural Dynamics (IFASD), Savannah, GA, USA, 9-13 June 2019*.

[9] Gustavsen, B. and Semlyen, A. (1999). Rational approximation of frequency domain responses by vector fitting. *IEEE Transactions on Power Delivery*, 14(3), 1052–1061. doi: 10.1109/61.772353.